

Microstructure-Driven Fracture Behaviors and Thermo-Mechanical Analysis of Large Area Additive Manufactured Short Fiber Composites

Douglas E. Smith*, Arief Yudhanto, Neshat Sayah

Department of Mechanical Engineering, Baylor University, Waco, TX 76706

ABSTRACT

Large area additive manufacturing (LAAM) of polymers and short carbon-fiber polymer composites have proven effective for producing meter-scale parts. Unfortunately, LAAM parts exhibit substandard strength due in part to process-induced microstructural defects, including microvoids within the printed beads. In this work, a comprehensive analysis incorporating experimental, empirical and numerical methods to study the effect of voids and fibers on bead properties, degree of healing, and fracture behaviors were performed on LAAM-produced acrylonitrile butadiene styrene (ABS) and short carbon fiber-reinforced ABS (CF/ABS). Compact tension specimens (CTS) measure interbead and crossbead fracture toughness K_{Ic} of ABS and CF/ABS. The correlation between residual stress and fracture behaviors in ABS and CF/ABS is established, providing a comprehensive set of tools and insights into the processing effects on LAAM part strength.

INTRODUCTION

Large area additive manufacturing (LAAM) is gaining popularity for producing large polymer composite structures due to its rapid execution. The LAAM process typically involves extruding molten polymer through heated nozzles onto a print bed, creating thermal gradients during cooling that can affect the adhesion between deposited beads [1]. These gradients may lead to residual stress, geometric distortions, and voids [2-5], which can compromise interbead adhesion and reduce the damage tolerance of finished parts. The higher thermal mass in LAAM beads results in slower cooling rates, causing the printed beads to compress under subsequent layers [6]. These challenges primarily impact materials made via LAAM compared to standard sized additive manufacturing [7-9]. Understanding the process-induced microstructural changes (i.e., fiber reorientation and void development) and their effects on thermomechanical behaviors and structural integrity is crucial for enhancing confidence in LAAM technology.

Microstructural features in LAAM short fiber composites have been studied by various authors, many of which have focused on the influence of voids and fibers on the mechanical properties [10-13]. Modeling approaches for analyzing LAAM polymer and polymer composites have also appeared. For example, transient thermal analyses have been used to evaluate the time-temperature history of bead stacks during material extrusion-deposition. Compton et al. developed a 1D transient thermal model for thin walls in LAAM-manufactured parts [14], while Owens et al. created a 2D finite volume model to evaluate FFF and LAAM thermal histories [1]. However, both models did not consider the actual shape, geometry, and microstructural features of the deposited beads.

Short fiber polymer composite beads produced by the LAAM process have been shown to have microstructures that are both inhomogeneous and non-isotropic where both fibers and microvoids vary over the bead cross section. Microvoid volume fraction varies with location within the bead, from bead to bead, and are seen within short fiber filled beads, but not within neat polymer beads [15,16]. Furthermore, fibers tend to align in the print direction and show much higher alignment around the outer edges of the bead. The center of the bead tends to have a much more random fiber alignment and more microvoids. It has been shown that there is an inverse correlation between fiber alignment and microvoid volume fraction in short carbon fiber ABS beads [15,17]. In separate studies, the interbead fracture toughness has been measured for various material and extrusion-deposition systems [18-22]. Most relevant to this paper is a study by Barocio [22] show showed that heating the print bed significantly increased the interbead fracture toughness. In addition, Yudhanto, et al., [23] showed that interbead fracture toughness improved further from a non-heated print bed, and that printed ABS beads had a significantly higher interbead and intrabead fracture toughness than carbon fiber ABS. These experiments help to better understand factors that affect fracture toughness, however, they do not address the effect that bead microstructure has on interbead adhesion.

This paper aims to (i) characterize the microstructural features (shape, geometry, void volume fraction, fiber orientation) of short carbon fiber-reinforced acrylonitrile butadiene styrene (CF/ABS) using X-ray computed tomography (X-ray μ CT), (ii) evaluate interbead mechanical adhesion via fracture toughness testing, (iii) create 2D thermo-mechanical finite element models with realistic bead geometries and thermal mechanical properties derived from μ CT-measured bead microstructures to simulate the transient thermal and residual stress history during the bead extrusion-deposition, and (iv) estimate the degree of healing of the deposited beads with realistic microstructures. This paper presents results from ongoing research that aims to better understand the effect of LAAM processing on polymer composite microstructure formation and its effect on structural integrity of LAAM parts.

METHODS

Materials and large area additive manufacturing

Neat acrylonitrile butadiene styrene (ABS) and short carbon fiber-reinforced ABS (CF/ABS) with 13 wt.% of carbon fibers were used to print large-area additive manufacturing (LAAM) single and multi-bead samples for evaluation and testing. Before the extrusion-deposition was performed, neat ABS and CF/ABS pellets were dried in an oven at 80 °C for 12 h. Single beads and multi-bead stacks of two, eight, and twenty-four layers with one-bead width (7-10 mm) were printed with the nozzle diameter of 3.17 mm and nozzle height (from the print bed) of 1.2 mm. The nozzle temperature was 220°C. The print bed and ambient temperature remained at room temperature (23°C) throughout processing. Each bead was deposited onto the print bed or previously printed beads and bead deposition was performed in the same direction at the time interval of 17 seconds. The screw speed was 90 rpm, while the nozzle flow rate and translation speed were 4.5 kg/h and 40 mm/s, respectively. To prepare fracture toughness test specimens, an initial crack was made in the double-bead configuration specimen by inserting a Teflon film with the thickness of 70 micron between the first and second printed bead. This pre-crack served as a starter to initiate the crack at the bead interface in both CF/ABS and ABS test samples.

X-ray micro-computed tomography

X-ray computed tomography was performed with the NSI X3000 μ CT (North Star Imaging, Rogers, MN, USA) to characterize the geometry, void content, and fiber orientation within the deposited LAAM beads. Only single-width eight-layer CF/ABS beads were scanned for this study where two resolution scans were performed with scan settings shown in **Table 1**. The *standard-resolution* scan setting was used to identify the 2D geometry of the beads, and the *high-resolution* scan was used to characterize the void volume fraction and fiber orientation within the bead.

Table 1. Parameters prescribed in X-ray computed tomography for characterizing bead microstructures produced by large-area additive manufacturing (LAAM)

Parameter	Standard-resolution scan	High-resolution scan
Voltage	60 kV	60 kV
Current	900 μ A	900 μ A
Projection number	1440	2400
Voxel size	10 μ m	1.7 μ m
Scan duration	75 min	348 min

Homogenization method

Thermo-elastic material constants of the short fiber polymer composites were computed using an orientation homogenization method, where properties are computed using measured fiber orientation tensor values following the procedure proposed by Advani and Tucker [24] and further developed by Jack and Smith [10]. This method treats the composite as a collection of representative volume elements (RVEs), each containing short fibers within a matrix phase and categorized into pseudo-grains. Each pseudo-grain maintains the same fiber and matrix volume fraction as the overall composite, with fibers sharing the same orientation. The approach involves two main steps: (i) calculation of the stiffness of each pseudo-grain by assuming unidirectional fiber alignment and uniform fiber length; (ii) homogenization of all pseudo-grains to determine the overall stiffness of composite system. The detailed mathematical treatment of thermal conductivity, elastic constants (based on the modified Halpin-Tsai technique), and coefficient of thermal expansion (CTE) can be reviewed in Refs. [17].

Finite element method

Finite element method (FEM) simulations using 2D 4 node continuum elements were performed with ABAQUS (Dassault Systemes, Waltham, MA, USA) to analyze the temperature distribution and residual stress during the deposition of multiple 3D-printed beads on an aluminum build plate. Each bead was deposited in the FEM simulation at 17-second intervals using the ABAQUS element birth feature, and the model was composed of 1,517 elements total (600 for the build plate and 917 for the beads). The actual geometry of the beads was obtained using standard-resolution μ CT, and coordinates were exported to MATLAB to create a 2D FE model. High-resolution scans of the first and fourth bead above the build platform provided microstructural data, which were used to compute material properties for the FEA models for the lower (bead 1 to bead 3) and upper beads (bead 4 to bead 8), respectively. It was seen that these sets of beads generally contained distinct properties, likely due to the difference in cooling rates which varied with distance from the build platform. Key physical characteristics of bead 1 and bead 4, such as

void volume fraction and orientation tensor components, are summarized in **Table 2**. Simulations were also performed for perfectly aligned ($A_{xx} = A_{yy} = 0$, $A_{zz} = 1$) and perfectly random ($A_{xx} = A_{yy} = A_{zz} = 1/3$) fiber orientations to provide insights into the effect of fiber alignment over a range of orientation tensor values that form practical limits on expected values. Computed values of degree of healing appear in the results section for these additional simulations.

Table 2. Physical characteristics of scanned CF/ABS beads

Bead position	volume fraction (%)	orientation tensor			Remark
		A_{xx}	A_{yy}	A_{zz}	
Bead-1	13%	0.17	0.12	0.71	employed for defining Bead 2 and Bead 3
Bead-4	10%	0.20	0.08	0.72	employed for defining Bead 5 to Bead 8

Computing the bead interface degree of healing

The bonding strength between beads was evaluated based on the time-dependent, non-isothermal degree of healing D_h which takes on values between 0 and 1, representing incomplete and complete bonding, respectively, and is given as [25]

$$D_h(t) = \frac{\sigma}{\sigma_\infty} = \left[\int_0^t \frac{1}{t_w(T)} \right]^{\frac{1}{4}} \quad (1)$$

where σ is the time-dependent bond strength between beads and σ_∞ is the strength of bulk material. The temperature-dependent welding time $t_w(T)$ for ABS is taken from [26] as

$$t_w(T) = 1.080 \times 10^{-47} \exp\left(\frac{Q_d}{RT}\right) \quad (2)$$

where Q_d is the activation energy for polymer diffusion, R is the universal gas constant (8.314 J/(mol·K)).

Fracture test methods

A double cantilever beam with doubler (DCB-D) test, as proposed by Yudhanto et al. [23], was employed to evaluate the Mode I (opening) critical strain energy release rate G_{Ic} of ABS and CF/ABS at intralayer and interlayer regions. G_{Ic} is the rate of energy that is being released due to the unit extension of crack within (intralayer) and between (interlayer) beads. Initial cracks were introduced by placing a PTFE film between the beads during printing, followed by a sharp crack tip being added with a blade. Doublers were bonded to the print bead samples using Scotch-Weld™ Structural Plastic Adhesive (3M™, Maplewood, MN, USA). All fracture toughness tests were conducted on a universal testing machine TestResources Model 100-1000-6 tensile test machine with a 4.4 kN load cell, (TestResources Inc., Shakopee, MN, USA) at a displacement rate of 1 mm/min. Crack lengths were recorded using a handheld microscope (Dino-Lite Edge,

Microscope LLC, Roanoke, VA). Values of G_{Ic} were calculated based on the Simple Beam Theory as

$$G_{Ic} = \frac{P^2 a^2}{b_f (EI)_T} \quad (3)$$

where P is the applied load, b_f is the sample width at the crack location, a is the distance from the applied load to the crack tip, and the total bending stiffness $(EI)_T$ is calculated as

$$(EI)_T = E_d(I_d + A_d|z_d - \bar{z}|^2) + E_s(I_s + A_s|z_s - \bar{z}|^2) \quad (4)$$

where E_d and E_s are the Young's modulus of the doubler and sample, respectively. The distance measured from the composite line (C_L) to the plane of crack propagation \bar{z} is given as

$$\bar{z} = \frac{(E_d/E_s)A_d z_d + A_s z_s}{(E_d/E_s)A_d + A_s} \quad (5)$$

The geometric parameters for the doublers (moment of inertia I_d , cross-sectional area A_d , and height from the neutral axis z_d) are given as

$$I_d = \frac{b_d h_d^3}{12}, \quad A_d = b_d h_d, \quad z_d = (h_s/2) + (h_d/2) \quad (6)$$

The geometric parameters for single-bead specimen (moment of inertia I_s , cross sectional area A_s , and distance from neutral axis z_s) are given as

$$I_s = \frac{b_f h_s^3}{96}, \quad A_s = \frac{b_f h_s}{2}, \quad z_s = h_s/2 \quad (7)$$

The geometric parameters for the double-bead specimen (area moment of inertia I_s , cross sectional area A_s , and distance from the neutral axis z_s) are given as

$$I_s = \frac{h_s^3}{32} \left(\frac{b_f}{3} + \frac{\pi h_s}{32} \right), \quad A_s = \frac{b_f h_s}{2} + \frac{\pi h_s^2}{16}, \quad z_s = h_s/4 \quad (8)$$

The standard compact tension specimen (CTS) was employed to measure G_{Ic} using the 24 layer multiple-bead test samples, which is calculated as

$$G_{Ic} = \frac{K_{Ic}^2}{E_s} (1 - \nu_s^2) \quad (15)$$

where ν_s is the sample Poissons Ratio and the stress intensity factor K_{Ic} is calculated as

$$K_{Ic} = \frac{P_{max}}{(b_f\sqrt{W})} \left(\frac{2+x}{1-x^{1.5}} \right) [0.886 + 4.64x - 13.32x^2 + 14.72x^3 - 5.6x^4] \quad (16)$$

and

$$x = a_0/W \quad (17)$$

where P_{max} is the maximum force during the test of CTS, W is the width of CTS, and a_0 is the distance between pin and crack tip.

RESULTS AND DISCUSSION

Microstructures of LAAM-printed ABS and CF/ABS beads

Figure 1 contains cross-sectional views of ABS and CF/ABS, respectively, obtained from high-resolution μ CT of LAAM printed bead stacks. **Figure 1a** shows that printed ABS beads have almost no voids, including at the bead-to-bead interface. In contrast, CF/ABS beads contain numerous voids around randomly oriented short fibers (cf. **Figure 2b**), with fiber and void volume fractions measured at 8.1% and 11.7%, respectively. Note that the pellets used to produce the CF/ABS (not shown) has a lower void volume fraction of 7.8%. The printing process appears to increase the void volume fraction in CF/ABS by 3.9%. In areas with randomly oriented fibers near the bead center, the void volume fraction was measured to be 17.1% which are significantly higher than the measured 8.3% void volume fraction near the edges of the bead. The same CF/ABS multi-bead stacks showed an interbead void volume of 11.7% which is expected to negatively affect bead adhesion.

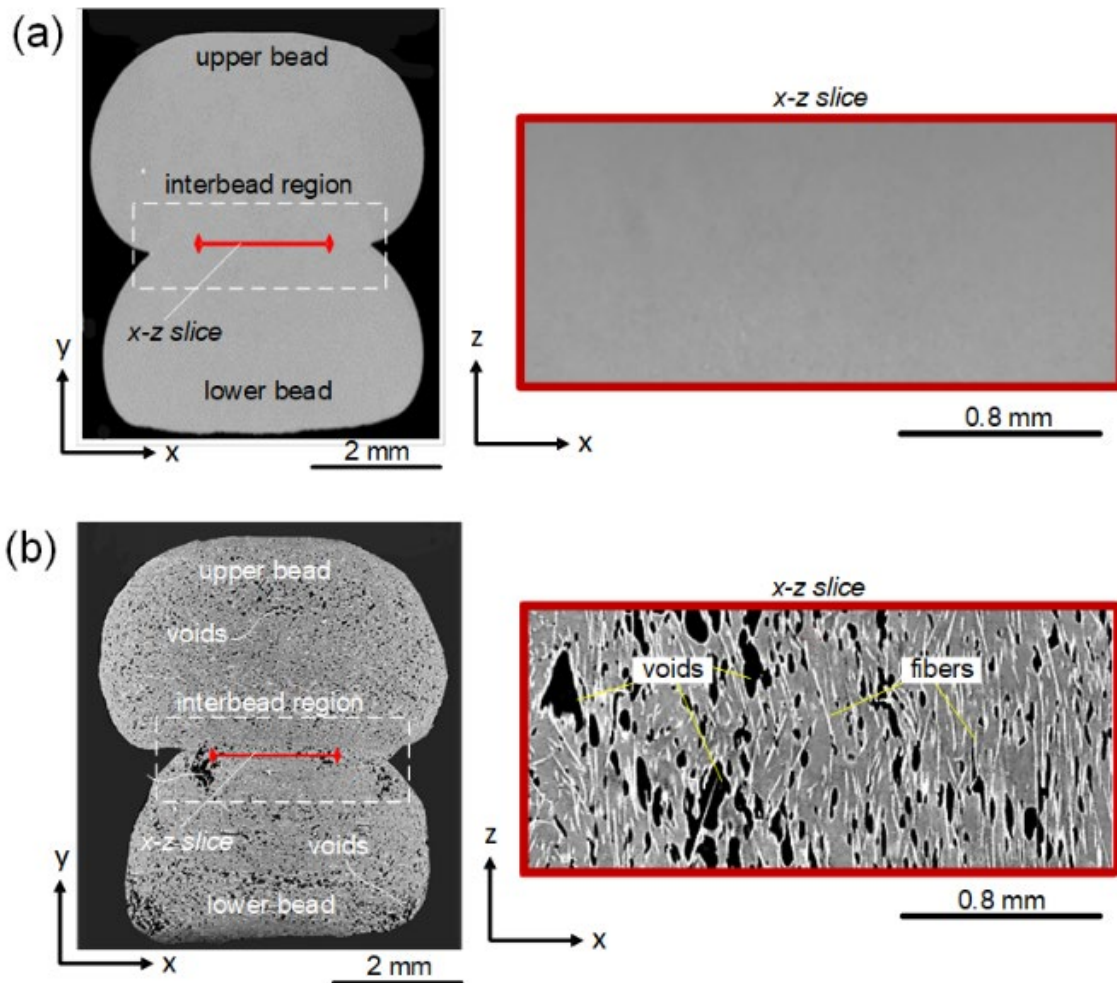


Figure 1. 2D X-ray micro-computed tomography images of two-bead systems printed using large area additive manufacturing machine: (a) ABS, (b) CF/ABS

Thermo-elastic constants

Homogenized thermal conductivity values appear in **Table 3** for ABS and CF/ABS for the various fiber orientation conditions considered in this study. Conductivities are provided for perfectly aligned, perfectly random, and for fiber orientations obtained from our μ CT measurements. **Table 3** shows that neat ABS and uniformly random fiber distributions yield isotropic thermal conductivities. However, other, nonuniform orientations result in higher thermal conductivity in the print direction since these samples also have fibers that show an increased alignment in that direction (i.e., in the z -direction). Note that thermal conductivity was assumed to be independent of temperature in our simulations.

Additional thermo-elastic constants for the same short fiber composite microstructures appear in **Table 4**. As with thermal conductivities, computed moduli illustrate the effect of bead microstructure, i.e., fiber orientation and void volume fraction, on calculated thermo-elastic properties (elastic moduli and coefficient of thermal expansion (CTE)) of the CF/ABS composites considered here. Note that **Table 4** presents the thermo-elastic properties of the materials obtained

at 80°C. The properties for neat ABS were computed based on the data provided in Ref. [20], while that for CF/ABS were computed using the homogenization process described above. The thermal stress simulations presented below also included temperature dependent properties for neat ABS (and also CF/ABS through the homogenization process) based data provided by Cattenone et al.

[27] who included elastic modulus as a function of temperature for ABS.

Table 3. Computed thermal properties for CF/ABS composite with various microstructures.

Simulation Microstructure	Density (kg/m ³)	Specific Heat (J/g°C)	Thermal Conductivity Matrix K (W/m°C)
Neat ABS	1040	2080	0.177
CF/ABS aligned fiber/no void	1095	2002	$\begin{bmatrix} 0.222 & 0 & 0 \\ 0 & 0.222 & 0 \\ 0 & 0 & 0.654 \end{bmatrix}$
CF/ABS aligned fiber/5%void	1040	1902	$\begin{bmatrix} 0.621 & 0 & 0 \\ 0 & 0.211 & 0 \\ 0 & 0 & 0.211 \end{bmatrix}$
CF/ABS aligned fiber/12%void	963	1762	$\begin{bmatrix} 0.195 & 0 & 0 \\ 0 & 0.195 & 0 \\ 0 & 0 & 0.575 \end{bmatrix}$
CF/ABS uniformed fiber/no void	1095	2002	$\begin{bmatrix} 0.366 & 0 & 0 \\ 0 & 0.366 & 0 \\ 0 & 0 & 0.366 \end{bmatrix}$
CF/ABS uniformed fiber/5%void	1040	1902	$\begin{bmatrix} 0.348 & 0 & 0 \\ 0 & 0.348 & 0 \\ 0 & 0 & 0.348 \end{bmatrix}$
CF/ABS uniformed fiber/12%void	963	1762	$\begin{bmatrix} 0.322 & 0 & 0 \\ 0 & 0.322 & 0 \\ 0 & 0 & 0.322 \end{bmatrix}$
CF/ABS μ CT results/13% void	953	1742	$\begin{bmatrix} 0.261 & 0 & 0 \\ 0 & 0.231 & 0 \\ 0 & 0 & 0.464 \end{bmatrix}$
CF/ABS μ CT results/10% void	985	1802	$\begin{bmatrix} 0.270 & 0 & 0 \\ 0 & 0.239 & 0 \\ 0 & 0 & 0.480 \end{bmatrix}$

Table 4. Computed thermo-elastic properties for CF/ABS composite with various microstructures at 80 °C.

Aligned fiber orientation ($A_{xx} = 0, A_{yy} = 0, A_{zz} = 1$)			
Properties	$\phi_v = 0$	$\phi_v = 5\%$	$\phi_v = 12\%$
E_x (MPa)	2542.2	2415.1	2237.1
E_y (MPa)	2541.5	2414.4	2236.5
E_z (MPa)	9248	8785.6	8139.2
E_{xy} (MPa)	1341.9	1274.8	1180.9
CTE _x ($10^{-6}/^{\circ}\text{C}$)	105.9	111.5	120.3
CTE _y ($10^{-6}/^{\circ}\text{C}$)	105.9	111.5	120.4
Uniform random fiber orientation ($A_{xx} = 1/3, A_{yy} = 1/3$ and $A_{zz} = 1/3$)			
Properties	$\phi_v = 0$	$\phi_v = 5\%$	$\phi_v = 12\%$
E_x (MPa)	3889.9	3695.4	3422.6
E_y (MPa)	3889.9	3695.4	3422.6
E_z (MPa)	3889.9	3695.4	3422.6
E_{xy} (MPa)	1778	1689.1	1523.2
CTE _x ($10^{-6}/^{\circ}\text{C}$)	54.3	57.2	61.7
CTE _y ($10^{-6}/^{\circ}\text{C}$)	54.3	57.2	61.7
μCT -based fiber orientation $\phi_v = 13\%$ ($A_{xx} = 0.17, A_{yy} = 0.12$ and $A_{zz} = 0.71$) $\phi_v = 10\%$ ($A_{xx} = 0.20, A_{yy} = 0.08$ and $A_{zz} = 0.72$)			
Properties	$\phi_v = 0$	$\phi_v = 10\%$	$\phi_v = 13\%$
E_x (MPa)	N/A	3007.9	2786.3
E_y (MPa)	N/A	2673.8	2476.8
E_z (MPa)	N/A	6327.7	5861.4
E_{xy} (MPa)	N/A	1400.6	1297.4
CTE _x ($10^{-6}/^{\circ}\text{C}$)	N/A	80.2	86.5
CTE _y ($10^{-6}/^{\circ}\text{C}$)	N/A	106.6	115.1

FEA computed thermal history during the extrusion-deposition process

Transient thermal FEA simulations of the LAAM bead deposition process for neat ABS and CF/ABS were performed on an 8 bead stack model assuming a nozzle and print bed temperature of 210°C and 23°C, respectively. Temperature contour plots (cf. **Figure 2**) show that the maximum temperature for the ABS bead consistently exceeds that of the CF/ABS bead throughout the deposition process. For example, at $t = 17$ s, the ABS bead cools to a maximum temperature of 149.7°C, while the same for the CF/ABS is 109.4°C. As deposition continues, the maximum temperatures at $t = 34$ s is 177.4°C for the ABS print while the CF/ABS has cooled to 147.9°C, indicating a higher rate of heat transfer to the relatively cold build plate for CF/ABS. The minimum temperatures calculated for both materials were similar, reflecting the influence of the cold build plate. **Figures 2a-b** also illustrate the transient temperature drop at the outer surface of the various bead interfaces, where the interface nodes at the outer surfaces exhibit a relatively higher thermal gradient as compared to those in the interior. As each new bead is added, the prior bead shows a slight rise in maximum temperature as expected. This temperature rise in the ABS model reaches a plateau after the fifth bead, while CF/ABS continues to show an increase in temperature with the addition of each new bead through the end of our simulation. Ultimately, the ABS beads cool more slowly than CF/ABS due to the latter having a higher thermal conductivity which is caused by the presence of carbon fiber, resulting in CF/ABS retaining heat for a shorter duration after deposition.

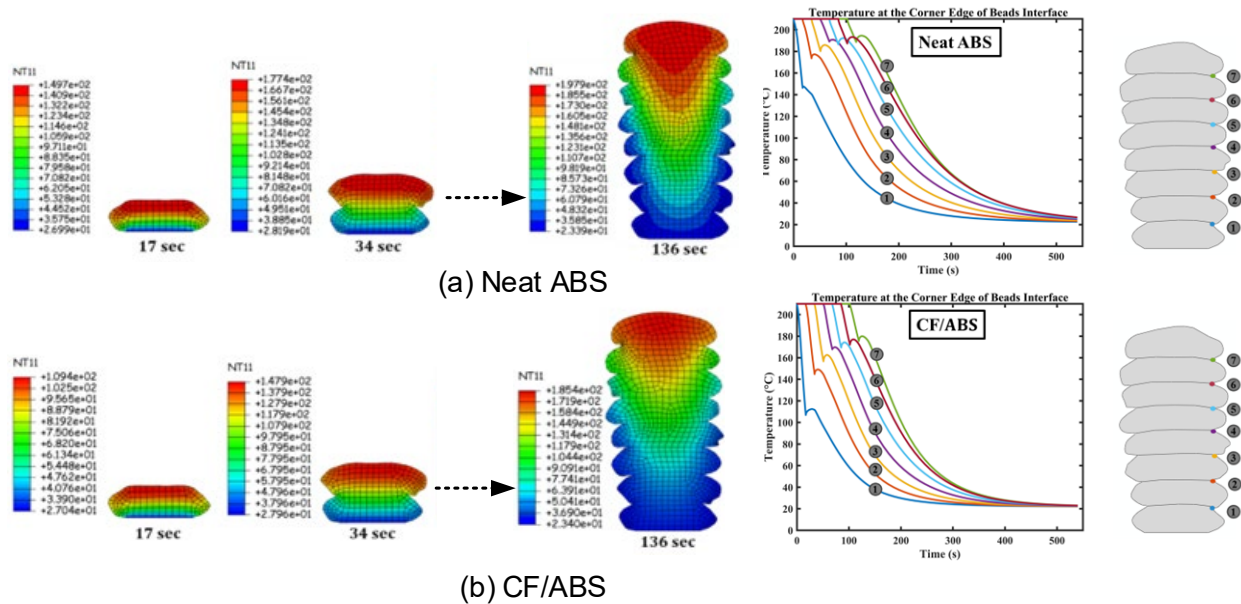


Figure 2. The temperature contour plot and nodal temperature obtained from FE analysis in (a) ABS, (b) CF/ABS.

Degree of healing at ABS and CF/ABS bead interfaces

The nodal temperature at the outer edged of the bead interface was used to calculate the degree of healing at the seven bead interfaces during deposition of the 8 bead stack FEM transient thermal simulations described above. As shown in **Figure 2**, the temperature at the bead 1-2 interface drops rapidly from 210°C to about 110°C and 150°C for the CF/ABS and ABS beads, respectively, within 17 s, resulting in a cooling rate of 212-424°C/min. Despite significant

increases in healing factors at greater distances from the print bed, **Figure 3a** shows that D_h at bead interface 1-2 remained below unity for all materials, indicating poor bonding due to the relatively high cooling rate in bead-1 (i.e., with temperatures at 150°C for ABS and 120°C for CF/ABS) and bead-2 (i.e., with temperatures at 175°C for ABS and 150°C for CF/ABS). As a result, the proximity of the bead 1-2 interface to the room-temperature print bed hinders interbead adhesion where we calculated $D_h = 0.83$ and $D_h = 0.06$ for neat ABS and CF/ABS, respectively. In contrast, D_h at interface 2-3 in ABS shows sufficient healing (i.e., $D_h \geq 1$), while that in

CF/ABS with aligned fibers also achieve $D_h \geq 1$ (see **Figure 3b**). As the interface location is moved farther away from the print bed, D_h is shown to attain unity in simulations except for CF/ABS with both uniform fibers and voids (see **Figure 3c**). At interface 4-5, D_h reached unity for all configurations (see **Figure 3d**). The findings indicate that aligned fibers enhance interfacial healing, while voids have a lesser impact. The addition of carbon fibers reduces bead temperature and interbead adhesion, while highly aligned fibers in the print direction increase bead temperature and improve adhesion as compared to uniformly distributed fibers. Voids decrease material density and further lower bead temperature, weakening adhesion.

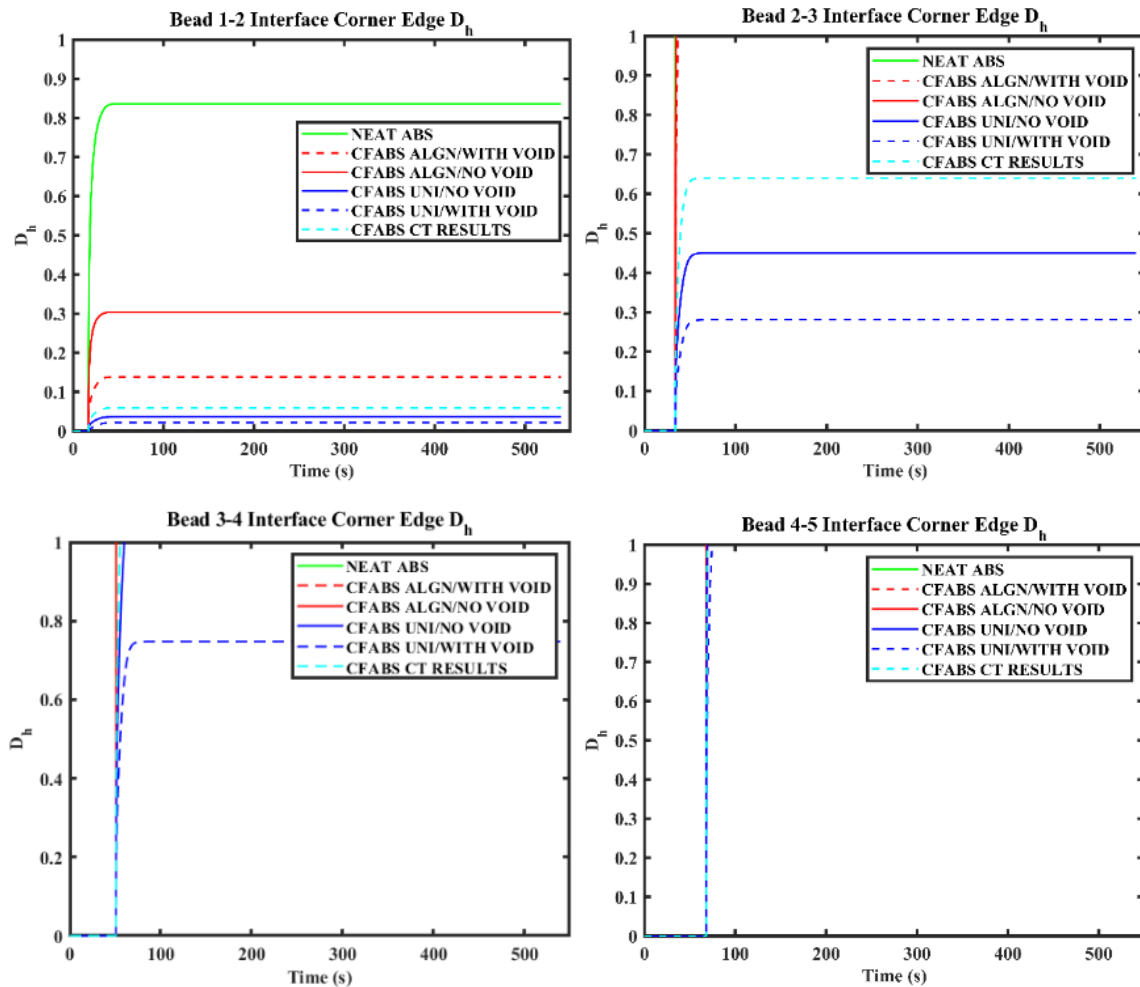


Figure 3. Estimated degree of healing at selected bead interfaces: (a) interface 1-2, (b) interface 2-3, (c) interface 3-4, (d) interface 4-5.

Figure 3 also includes calculated results for bead systems with perfectly aligned and perfectly random using thermal conductivities from **Table 3**. It was determined that the cooling rate for neat ABS was much slower than that of CF/ABS which resulted in bead interfaces remaining at higher temperatures longer for ABS as compared to CF/ABS, thus increasing the degree of healing. It was also shown that the decreased cooling rate within beads further from the build platform also results in increased adhesion. In summary, the presences of carbon fiber, the random orientation of carbon fiber, and the presence of voids all decreased adhesion.

Thermo-Elastic Stress

The coupled thermo-mechanical simulation based on material properties in **Tables 3 and 4** showed that the relatively higher elastic moduli and cooling rates in CF/ABS promoted higher residual stresses as compared to neat ABS which is shown in **Figure 4**. In addition, the locations of high residual tensile stress were shown to be in areas of high void content which is expected as the outer shell of the bead tends to become more ridged first putting the bead interior material under tension as it contracts during continued cooling.

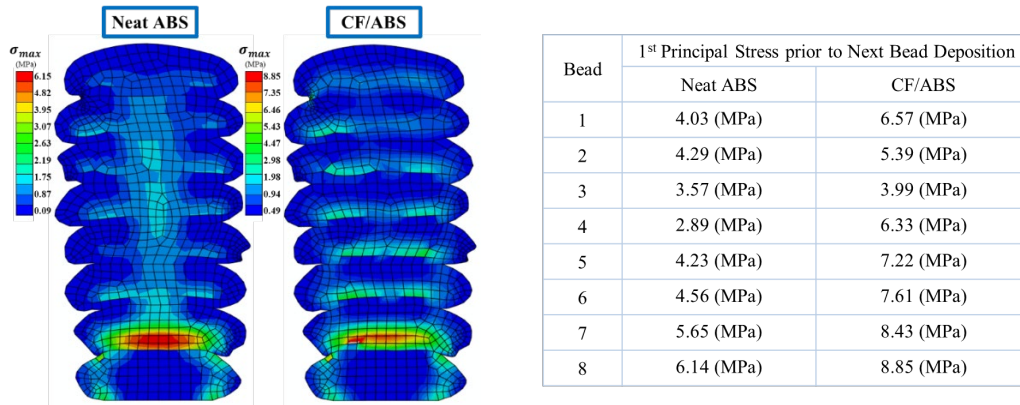


Figure 4. Calculated Von Mises stress within printed beads of ABS and CF/ABS determined through a transient thermo-mechanical simulation of LAAM bead deposition

Fracture behaviors

The effect of degree of healing on the quality of bead adhesion was assessed by analyzing the interbead fracture properties, i.e., critical strain energy release rate G_{IC} at various locations in the LAAM printed bead stacks. **Table 5** shows the measured intrabead and interbead G_{IC} of neat ABS and CF/ABS. The single-bead specimens were used to produce intrabead G_{IC} which were found to be lower as compared to neat ABS, especially at the initiation stage, which is attributed to the presence of voids acting as crack initiators in the CF/ABS samples. The maximum measured G_{IC} in CF/ABS was higher than that in ABS due to the fiber pull-out that provided additional energy dissipation during the intrabead fracturing process. In double and multi-bead configurations, ABS exhibited significantly higher interbead adhesion than CF/ABS due in part to the relatively lower number of voids present in the ABS sample. Note that the calculated degree of healing was found to be poorer near the print bed (i.e., $D_h = 0.83$ and 0.06 for neat ABS and CF/ABS, respectively), and improved adhesion was observed with distance from the print bed (i.e., the computed D_h exceeded unity for both neat ABS and CF/ABS) which is consistent with the high measured G_{IC} values obtained from multi-bead specimens.

Table 5. The strain energy release rate G_{Ic} measured in intrabead and interbead of ABS and CF/ABS using single-bead, double-bead, and multi-bead test specimens.

Fracture orientation	Specimen type	G_{Ic} (J/m ²) Initiation		G_{Ic} (J/m ²) Maximum	
		ABS	CF/ABS	ABS	CF/ABS
Intrabead	Single-bead	270	90	600	1060
Interbead	Double-bead	150	80	1170	770
Interbead	Multi-bead	2420	590	-	-

CONCLUSIONS

This paper presents a framework for analyzing the effects of microstructural features, such as fiber orientation and voids, on the thermal behavior and fracture properties of large-area additive manufactured short fiber composites using X-ray computed tomography. A two-dimensional transient thermal finite element analysis revealed that neat ABS beads maintain higher temperatures than CF/ABS beads after deposition, due to the enhanced thermal conductivity from the carbon fibers in CF/ABS, which results in faster cooling. The study also found that carbon fibers lower bead temperature and reduce interbead healing. In addition, fiber orientation was shown to significantly effect predicted adhesion as random fiber distributions yielded lower adhesion as compared to uniaxial alignment. Voids in CF/ABS composites increase maximum principal stress and reduce adhesion (critical energy release rate), though fiber orientation plays a more crucial role in stress variation, with unidirectional alignment leading to higher anisotropic behavior.

ACKNOWLEDGEMENT

The authors would like to thank Baylor University, United States for its financial support throughout the research work. We also thank the National Science Foundation (Award Number 2055628) for the financial support.

REFERENCES

- [1] J. T. Owens, A. Das, and M. J. Bortner, "Accelerating heat transfer modeling in material extrusion additive manufacturing: From desktop to big area," *Addit. Manuf.*, vol. 55, p. 102853, Jul. 2022, doi: 10.1016/j.addma.2022.102853.
- [2] B. G. Compton, B. K. Post, C. E. Duty, L. Love, and V. Kunc, "Thermal analysis of additive manufacturing of large-scale thermoplastic polymer composites," *Addit. Manuf.*, vol. 17, pp. 77–86, Oct. 2017, doi: 10.1016/j.addma.2017.07.006.
- [3] M. R. Talagani, S. DorMohammadi, R. Dutton, C. Godines, H. Baid, and F. Abdi, "Numerical Simulation of Big Area Additive Manufacturing (3D Printing) of a Full Size Car," *SAMPE J.*, vol. 51, no. 4, 2015.

- [4] T. D'Amico and A. M. Peterson, "Bead parameterization of desktop and room-scale material extrusion additive manufacturing: How print speed and thermal properties affect heat transfer," *Addit. Manuf.*, vol. 34, p. 101239, Aug. 2020, doi: 10.1016/j.addma.2020.101239.
- [5] A. Roschli et al., "Designing for Big Area Additive Manufacturing," *Addit. Manuf.*, vol. 25, pp. 275–285, Jan. 2019, doi: 10.1016/j.addma.2018.11.006.
- [6] K. Choo et al., "Heat retention modeling of large area additive manufacturing," *Addit. Manuf.*, vol. 28, pp. 325–332, Aug. 2019, doi: 10.1016/j.addma.2019.04.014.
- [7] M. Pourali and A. M. Peterson, "Thermal Modeling of Material Extrusion Additive Manufacturing," in *ACS Symposium Series*, vol. 1315, J. E. Seppala, A. P. Kotula, and C. R. Snyder, Eds., Washington, DC: American Chemical Society, 2019, pp. 115–130. doi: 10.1021/bk-2019-1315.ch007.
- [8] K. Coasey, K. R. Hart, E. Wetzal, D. Edwards, and M. E. Mackay, "Nonisothermal welding in fused filament fabrication," *Addit. Manuf.*, vol. 33, p. 101140, May 2020, doi: 10.1016/j.addma.2020.101140.
- [9] M. Roy, R. Yavari, C. Zhou, O. Wodo, and P. Rao, "Prediction and Experimental Validation of Part Thermal History in the Fused Filament Fabrication Additive Manufacturing Process," *J. Manuf. Sci. Eng.*, vol. 141, no. 12, p. 121001, Dec. 2019, doi: 10.1115/1.4045056.
- [10] D. A. Jack and D. E. Smith, "Elastic Properties of Short-fiber Polymer Composites, Derivation and Demonstration of Analytical Forms for Expectation and Variance from Orientation Tensors," *J. Compos. Mater.*, vol. 42, no. 3, pp. 277–308, Feb. 2008, doi: 10.1177/0021998307086388.
- [11] B. P. Heller, D. E. Smith, and D. A. Jack, "Effects of extrudate swell and nozzle geometry on fiber orientation in Fused Filament Fabrication nozzle flow," *Addit. Manuf.*, vol. 12, pp. 252–264, Oct. 2016, doi: 10.1016/j.addma.2016.06.005.
- [12] B. P. Heller, D. E. Smith, and D. A. Jack, "Planar deposition flow modeling of fiber filled composites in large area additive manufacturing," *Addit. Manuf.*, vol. 25, pp. 227–238, Jan. 2019, doi: 10.1016/j.addma.2018.10.031.
- [13] T. Russell, B. Heller, D. Jack, and D. Smith, "Prediction of the Fiber Orientation State and the Resulting Structural and Thermal Properties of Fiber Reinforced Additive Manufactured Composites Fabricated Using the Big Area Additive Manufacturing Process," *J. Compos. Sci.*, vol. 2, no. 2, p. 26, Apr. 2018, doi: 10.3390/jcs2020026.
- [14] B. G. Compton, B. K. Post, C. E. Duty, L. Love, and V. Kunc, "Thermal analysis of additive manufacturing of large-scale thermoplastic polymer composites," *Addit. Manuf.*, vol. 17, pp. 77–86, Oct. 2017, doi: 10.1016/j.addma.2017.07.006
- [15] N. Sayah. "X-Ray Micro Computed Tomography-Based Characterization of Bead Microstructure in Polymer Composite Large Area Additive Manufacturing: Analysis, Simulation, and Experimentation," Ph.D. Thesis, Mechanical Engineering Department, Baylor University, 2024.

- [16] N. Sayah and D.E. Smith, “Effect of Process Parameters on Void Distribution, Volume Fraction, and Sphericity Within the Bead Microstructure of Large Area Additive Manufacturing Polymer Composites”, *Polymers in Special Issue on New Developments in Fiber Reinforced Polymer Materials*, 14:23, 5107, November, 2022, doi: 10.3390/polym14235107.
- [17] N. Sayah and D.E. Smith, “Correlation of Microstructural Features within Short Carbon Fiber/ABS Manufactured via Large Area Additive Manufacturing Beads: An Experimental Study”, *Jn of Composite Science*, 8:7, 246, 2024, doi: 10.3390/jcs8070246.
- [18] R. J. Rodriguez JF, Thomas JP, “Maximizing the strength of fused-deposition abs plastic parts”, in: *10th Solid Freeform Fabrication*, Austin, TX, 1999.
- [19] K. R. Hart, E. D. Wetzel, “Fracture behavior of additively manufactured acrylobutadiene styrene (abs) materials”, *Engineering Fracture Mechanics* 177 (2017) 1–13.
- [20] P. Rezaeian, M. R. Ayatollahi, A. Nabavi-Kivi, N. Razavi, “Effect of printing speed on tensile and fracture behavior of abs specimens produced by fused deposition modeling”, *Engineering Fracture Mechanics* 266 (2022) 108393.
- [21] V. Kishore, C. Ajinjeru, A. Nycz, B. Post, J. Lindahl, V. Kunc, C. Duty, “Infrared preheating to improve interlayer strength of big area additive manufacturing (baam) components”, *Additive Manufacturing* 14 (2017) 7–12.E.
- [22] Barocio, B. Brenken, A. Favaloro, R. B. Pipes., “Interlayer fusion bonding of semi-crystalline polymer composites in extrusion deposition additive manufacturing”, *Composites Science and Technology* 230 (2022) 109334, *Recent Advances in Composites Science & Technology – A special issue in memoriam Prof. Dr.-Ing. Dr. h.c. mult. Klaus Friedrich*.
- [23] A. Yudhanto, N. Sayah, D.E. Smith, “Intrabead and interbead fracture analysis of large area additive manufactured polymer and polymer composites,” *Composites Science and Technology* 266, 111173, 2025
- [24] S. G. Advani and C. L. Tucker, “The Use of Tensors to Describe and Predict Fiber Orientation in Short Fiber Composites,” *J. Rheol.*, vol. 31, no. 8, pp. 751–784, Nov. 1987, doi: 10.1122/1.549945.
- [25] F. Yang and R. Pitchumani, “Healing of Thermoplastic Polymers at an Interface under Nonisothermal Conditions,” *Macromolecules*, vol. 35, no. 8, pp. 3213–3224, Apr. 2002, doi: 10.1021/ma010858o.
- [26] S. F. Costa, F. M. Duarte, and J. A. Covas, “Estimation of filament temperature and adhesion development in fused deposition techniques,” *J. Mater. Process. Technol.*, vol. 245, pp. 167–179, Jul. 2017, doi: 10.1016/j.jmatprotec.2017.02.026.
- [27] A. Cattenone, S. Morganti, G. Alaimo, and F. Auricchio, “Finite Element Analysis of Additive Manufacturing Based on Fused Deposition Modeling: Distortions Prediction

and Comparison with Experimental Data,” J. Manuf. Sci. Eng., vol. 141, no. 1, p. 011010, Jan. 2019, doi: 10.1115/1.4041626.